

Lipid domain coarsening and fluidity in multicomponent lipid vesicles: A continuum based model and its experimental validation

Y. Wang^{1,†}, Y. Palzhanov^{2,†}, A. Quaini², M. Olshanskii^{2,*}, S. Majd^{1,*}

November 5, 2021

¹Department of Biomedical Engineering, University of Houston, 3551 Cullen Blvd, Houston TX 77204

ywang147@uh.edu; smajd9@central.uh.edu

²Department of Mathematics, University of Houston, 3551 Cullen Blvd, Houston TX 77204
ypalzhanov@uh.edu; aquaini@uh.edu; maolshanskiy@uh.edu

[†] Equal contribution

^{*} Corresponding authors

Abstract Liposomes that achieve a heterogeneous and spatially organized surface through phase separation have been recognized to be a promising platform for delivery purposes. However, their design and optimization through experimentation can be expensive and time-consuming. To assist with the design and reduce the associated cost, we propose a computational platform for modeling membrane coarsening dynamics based on the principles of continuum mechanics and thermodynamics. This model couples phase separation to lateral flow and accounts for different membrane fluidity within the different phases, which is known to affect the coarsening dynamics on lipid membranes. The simulation results are in agreement with the experimental data in terms of liquid ordered domains area fraction, total domains perimeter over time and total number of domains over time for two different membrane compositions (DOPC:DPPC with a 1:1 molar ratio with 15% Chol and DOPC:DPPC with a 1:2 molar ratio with 25% Chol) that yield opposite and nearly inverse phase behavior. This quantitative validation shows that the developed platform can be a valuable tool in complementing experimental practice.

Keywords: Multicomponent Membranes; Membrane fluidity; Membrane Phase Separation; Computational Modeling; Fluorescence Microscopy; Liposomes

1 Introduction

Biological membranes are heterogenous and this characteristic is critical for their functionality. The lipid bilayer in these membranes hosts a variety of lipid species that may be organized into one of the two phases: liquid disordered and liquid ordered [42]. The tight packing of saturated lipids and cholesterol in the liquid ordered phase, in contrast to the loosely packed unsaturated lipids present in the liquid disordered phase leads, under certain conditions, to the lipid phase separation in membranes [7]. The liquid ordered domains - also known as lipid rafts - that are surrounded with liquid disordered phase in biological membranes, have been recognized as a key platform for cell signaling and membrane trafficking among other cellular processes [7, 6, 24, 3, 38]. Thus, these domains have received growing interest in the past few decades and have been the focus of numerous experimental and theoretical studies [22, 5].

More recently, domain formation on membranes has also been utilized to create novel membrane-based materials with heterogenous surfaces. When explored for drug delivery applications, these heterogenous membrane materials showed clear advantage over their homogenous membrane counterparts [4, 33]. With the increasing number of available lipid-conjugated molecules (e.g. peptides, polymers, etc), lipid membranes with heterogenous and spatially-organized surfaces can open new avenues for the design of novel materials. However, efficient design of such heterogenous membrane-based materials requires computer-aided modeling that can predict the lipid domain formation and dynamics on a given membrane composition in a reliable and quantitative manner. As a step towards addressing this need, we recently developed a computationally efficient method based on the surface Cahn–Hilliard phase-field model to predict the phase behavior and domain formation on ternary membrane compositions and we validated this continuum-based model using experiments [46]. In this study, we aim to further advance this computational platform to offer an enhanced and more accurate prediction of membrane phase separation.

Our current understanding of membrane phase separation is mainly based on the experimental studies performed on model membranes with well-defined lipid compositions. Amongst these model membranes, giant unilamellar vesicles (GUVs) have provided a particularly suitable platform for studying membrane phase behavior as their free-standing lipid bilayer closely mimics the natural membranes and their large size (micron-scale) makes them resolvable under optical microscopy [44]. The combinatorial use of GUVs and advanced fluorescence-based microscopy techniques have, for instance, shaped our knowledge on membrane domains’ thermodynamic equilibria [41, 11] and their coarsening dynamics [37]. These studies have also provided us with an insight into the distinct characteristics (e.g. morphology and fluidity) of liquid ordered and liquid disordered phases [16, 34, 35].

It has been demonstrated that membrane fluidity within the liquid ordered domains can be substantially lower than that in the liquid disordered phase [35]. Such a difference can affect the coarsening dynamics of rafts on membranes [37]. This interesting aspect of lipid domains was not considered in our previous study [46] as fluidity is not accounted for in the Cahn–Hilliard model. In order to enable more accurate predictions on membrane phase behavior with consideration of

membrane viscosity differences between liquid ordered and disordered phases, herein we apply a more complex model, the Navier–Stokes–Cahn–Hilliard model, along with a set of innovative numerical methods, to present an advanced computational platform for modeling membrane phase separation. To validate this model, we compare its numerical results to our experimental results on GUVs with ternary membrane compositions. Specifically, we apply fluorescence microscopy to examine the phase separation on GUVs with two distinct compositions (with opposite and nearly inverse phase behavior) and monitor the number of lipid domains, area fraction and perimeter over time and compare these results to those from our computational model.

2 Materials and methods

2.1 Experimental approach

2.1.1 Materials

Lipids 1,2-dioleoyl-sn-glycero-3-phosphocholine (DOPC), 1,2-dipalmitoyl-sn-glycero-3-phosphocholine (DPPC), 1,2-dipalmitoyl-sn-glycero-3-phosphoethanolamine-N- (lissamine rhodamine B sulfonyl) (Rho-PE) were purchased from Avanti Polar Lipids (Alabaster, AL). We purchased the sucrose from VWR (West Chester, PA). Cholesterol was from Sigma Aldrich (Saint Louis, MO) and chloroform from Omnipure (Caldwell, Idaho). Naphtho[2,3-a]pyrene (NAP) was from Thermo Fisher Scientific (Waltham, MA). All lipid stock solutions were prepared in chloroform. Indium tin oxide (ITO) coated glasses and microscope glass slides were from Thermo Fisher Scientific (Waltham, MA) and coverslips were from Corning Inc. (Corning, NY). ITO plates were cleaned using chloroform, ethanol and DI water prior to use. Microscope slides and coverslips were cleaned with ethanol and DI water before usage.

2.1.2 Preparation of Giant Unilamellar Vesicles (GUVs)

GUVs were prepared using a modified version of electroformation technique described in our previous studies [26, 30, 46]. In brief, an aqueous dispersion of small vesicles was used to produce dried lipid films on two ITO plates that later sandwiched a thin PDMS frame, creating an electroformation chamber. A sucrose solution (235 mM) was injected into the chamber to rehydrate the lipid films. Next, an AC electric field was applied while the chamber was placed in an oven ($\sim 60^\circ\text{C}$) to exceed the melting temperature of the used lipids. With a 50 Hz frequency, the electric field was increased to 2 Vpp at rate of 100 mVpp/min and held for ~ 3 hours using a function waveform generator (4055, BK Precision, Yorba Linda, CA) upon formation, GUVs were detached by decreasing the frequency to 1 Hz for ~ 30 min.

The above-mentioned small vesicles were prepared using dehydration-rehydration followed by tip-sonication as described in our prior studies [17, 46]. A mixture of DOPC, DPPC, and Chol plus 0.3 mol% Rho-PE and 0.5% NAP was prepared in chloroform and used to produce a thin lipid

film in a pearl-shaped flask using a rotary evaporator (Hei-Vap, Heidolph, Germany). The lipid film was then rehydrated using DI water (at $\sim 60^\circ\text{C}$) with a 2.5 mg/ml lipid concentration. The resultant milky suspension was tip-sonicated to produce a clear suspension of small vesicles.

Lipid compositions applied in this study were (i) DOPC: DPPC with a 1:1 molar ratio and 15% Chol, referred to as 1:1:15% composition, and (ii) DOPC: DPPC with a 1:2 molar ratio and 25% Chol, referred to as 1:2:25% composition. We included Rho-PE and NAP in both compositions to enable fluorescence microscopy.

2.1.3 GUV Imaging and Analysis

GUV imaging and characterization was performed as described before [46]. Briefly, GUVs were harvested from the electroformation chamber and placed on a clean microscope glass slide for imaging. Images were acquired using a Zeiss LSM 800 confocal laser scanning microscope (Zeiss, Germany). Prior to imaging, the sample was heated on a hot plate to $\sim 60^\circ\text{C}$ for 5 min and then placed on the microscope stage where it gradually cooled down to the room temperature. The image collection time was recorded with time zero considered as when the sample was removed from the hot plate. Epi-fluorescence microscopy was used for the initial assessment of GUVs and their lipid domains while confocal microscopy was used to further assess the domains on GUVs and quantify their size. Epi-fluorescence images were collected using a 40X objective with numerical aperture (NA) of 0.95, with 545/488 excitation wavelength and 572/509 emission wavelength. Confocal images were collected using a 63X oil objective with NA of 1.40 using 488 nm and 561 nm wavelength laser. Confocal image slices were collected with 0.4-0.9 μm Z-steps, depending on the size of the examined GUV, to minimize the time required for imaging the entire vesicle without significant movement of vesicle. Confocal images were analyzed using ZEN software (ZEN 2.6 lite, Zeiss, Germany).

Considering that Rho-PE and NAP have shown preferential partitioning to the liquid disordered phase and liquid ordered phase [15, 18], respectively, we assumed that green patches on the examined GUVs represented the liquid ordered phase while the red regions represented the liquid disordered phase.

For image-based characterization of GUVs, we assumed that the GUVs were perfect spheres and that the lipid domains on GUVs were in the form of spherical caps. For each GUV, all collected confocal image slices of each GUV were analyzed to find the vesicle diameter and surface area, as well as the surface area and perimeter of the lipid domains as detailed in [46]. We performed this analysis on 20 GUVs with 1:2:25% composition and 18 GUVs with 1:1:15% composition from at least 3 independent experiments per composition.

2.2 Computational approach

2.2.1 Mathematical model

In order to model phase separation, viscous and fluidic phenomena occurring in the GUV membrane, we consider a suitable modification [29] of a well-known thermodynamically consistent Navier–Stokes–Cahn–Hilliard (NSCH) model [1]. Let Γ be a sphere representing a liposome with a 10 μm diameter and let c_i be a fraction of elementary surface area occupied by phase i , with $i = 1, 2$. We choose $c = c_1$, $c \in [0, 1]$, as the representative surface fraction, e.g. the fraction of the ordered phase. Let ρ_1 and ρ_2 be the densities and η_1 and η_2 the dynamic viscosities of the two phases. Then, the density and viscosity of the mixture can be written as $\rho = \rho(c) = \rho_1 c + \rho_2(1 - c)$ and $\eta = \eta(c) = \eta_1 c + \eta_2(1 - c)$. Finally, let \mathbf{u} be the averaged tangential velocity in the mixture, p the thermodynamic interfacial pressure, and μ the chemical potential.

The NSCH system that governs the evolution of c , \mathbf{u} , p , and μ in time t and space $\mathbf{x} \in \Gamma \subset \mathbb{R}^3$ is given by:

$$\underbrace{\rho(\partial_t \mathbf{u} + (\nabla_\Gamma \mathbf{u})\mathbf{u})}_{\text{inertia}} - \underbrace{\text{div}_\Gamma(2\eta E_s(\mathbf{u})) + \nabla_\Gamma p}_{\text{lateral stresses}} = \underbrace{-\sigma_\gamma \epsilon^2 \text{div}_\Gamma(\nabla_\Gamma c \otimes \nabla_\Gamma c)}_{\text{line tension}} + \underbrace{M\theta(\nabla_\Gamma(\theta \mathbf{u}))\nabla_\Gamma \mu}_{\text{chemical momentum flux}} \quad (1)$$

$$\underbrace{\text{div}_\Gamma \mathbf{u}}_{\text{membrane inextensibility}} = 0 \quad (2)$$

$$\underbrace{\partial_t c + \text{div}_\Gamma(c\mathbf{u})}_{\text{transport of phases}} - \underbrace{\text{div}_\Gamma(M\nabla_\Gamma \mu)}_{\substack{\text{phase masses exchange} \\ \text{Fick's law}}} = 0, \quad \mu = \underbrace{f'_0(c) - \epsilon^2 \Delta_\Gamma c}_{\text{mixture free energy variation}} \quad (3)$$

on Γ for $t \in (0, t^{\text{final}}]$. In eq. (1)–(3), ∇_Γ stands for the tangential gradient, Δ_Γ for the Laplace–Beltrami operator, $E_s(\mathbf{u}) = \frac{1}{2}(\nabla_\Gamma \mathbf{u} + (\nabla_\Gamma \mathbf{u})^T)$ is the Boussinesq–Scriven strain-rate tensor, and div_Γ is the surface divergence. Eq. (3) provides the definition of the chemical potential, with $f_0(c) = \frac{1}{4}c^2(1 - c)^2$ being the double-well thermodynamic potential and parameter $\epsilon > 0$ representing the width of the (diffuse) interface between the phases. In addition, σ_γ is line tension coefficient, M is the mobility coefficient (see [21]), and $\theta^2 = \frac{d\rho}{dc}$. Problem (1)–(3) models the total exchange of matter between phases (eq. (3)) with surface flow described in terms of momentum conservation (eq. (1)) and area preservation (eq. (2)). Finally, problem (1)–(3) needs to be supplemented with initial values of velocity \mathbf{u}_0 and state c_0 . Here, we take $c_0 = c_0(\mathbf{x})$ corresponding to a homogeneous mixture and $\mathbf{u}_0 = \mathbf{0}$ (surface fluid at rest).

Several experimental works help with the settings of viscosity [32] and line tension [14, 19, 20]. For density, we calculated the value for each phase using the estimated molecular weight and molecular surface area for the corresponding phase (see supplementary material for details). Table 1 reports the values or range of values for such parameters for both compositions under consideration at two temperatures related to our experiments.

It is known that the dependence of the mobility and the phase-field parameter c produces important changes during the coarsening process [47]. In the absence of studies on the appropriate

Composition (Temp)	ρ_{l_o}	ρ_{l_d}	η_{l_o}	η_{l_d}	σ_γ
1:2:25% (15°C)	14.67	11.75	$5 - 8 \cdot 10^{-8}$	$0.2 - 0.4 \cdot 10^{-8}$	1.2 - 1.8
1:2:25% (17.5°C)	14.35	11.72	$5 - 8 \cdot 10^{-8}$	$0.2 - 0.4 \cdot 10^{-8}$	1.2 - 1.8
1:1:15% (22.5°C)	14.01	11.72	$0.43 - 5.7 \cdot 10^{-8}$	$0.2 - 0.4 \cdot 10^{-8}$	1.2 - 1.6
1:1:15% (25°C)	13.69	11.84	$0.43 - 5.7 \cdot 10^{-8}$	$0.2 - 0.4 \cdot 10^{-8}$	1.2 - 1.6

Table 1: Calculated value or range of values for the density of liquid ordered ($\rho_1 = \rho_{l_o}$) and liquid disordered ($\rho_2 = \rho_{l_d}$) phases in g/(mol·Å³), viscosity of liquid ordered ($\eta_1 = \eta_{l_o}$) and liquid disordered ($\eta_2 = \eta_{l_d}$) phases in Pa·s·m, and line tension in pN for the two membrane compositions at different temperatures. See supplementary material for details on the density calculations.

mobility function for lateral phase separation in liposomes, we consider degenerate mobility of the form $M = Dc(1 - c)$, which is a popular choice for analytical and numerical studies. Here, $D > 0$ is a diffusivity constant.

Parameter ϵ in the definition of the mixture free energy defines the width of transition layer between ordered and disordered phases. The transition layer width found in [31] is about 5 nm. Since a typical diameter of a spherical GUV in our experiments is 10 µm, the transition layer width can be estimated as 0.1% of its radius. This is beyond the capabilities of discrete continuum model which requires the resolution of layer by the mesh. In experiments we let $\epsilon = 0.1$ µm. This can be interpreted as letting tension forces act in a wider strip between phases, while preserving the produced momentum. Finally, the mobility coefficient M is a *modeling* parameter that determines the rate of change of the order indicator c depending on the specific free energy fluctuations. In [46], we estimated D to be in the range of $10^{-5}(\text{cm})^2\text{s}^{-1} - 2.5 \cdot 10^{-5}(\text{cm})^2\text{s}^{-1}$ depending on membrane composition. For numerical simulations presented in Sec. 3, we set $D = 10^{-5}(\text{cm})^2\text{s}^{-1}$.

In order to model an initially homogenous liposome, the surface fraction c_0 is defined as a realization of Bernoulli random variable $c_{\text{rand}} \sim \text{Bernoulli}(a_{\text{ld}})$ with mean value a_{ld} , where a_{ld} denotes lipid domain area fraction, i.e. we set:

$$c_0 := c_{\text{rand}}(\mathbf{x}) \quad \text{for active mesh nodes } \mathbf{x}. \quad (4)$$

Following the thermodynamic principles described in our previous work [46], we set $a_{\text{ld}} = 0.71$ for the 1:2:25% (DOPC:DPPC:Chol) composition and $a_{\text{ld}} = 0.29$ for the 1:1:15% composition.

2.2.2 Numerical method and input data

In order to find solutions to the NSCH problem in a generic setting, one has to resort to numerical methods. We discretize problem (1)-(3) with the trace finite element method (Trace FEM), a state-of-the-art computational technique for systems of partial differential equations (PDEs) posed on surfaces [28]. The first step in the application of Trace FEM is common to other finite element

methods. One writes an equivalent integral form of the PDE system, also known in PDE theory (see, e.g. [10]) as weak formulation. The weak formulation is obtained by multiplying the equations by smooth test functions, integrating the equations over Γ , and applying the surface Stokes formula. See [29] for the weak form of a reformulation of problem (1)-(3), that uses auxiliary pressure $\tilde{p} = p + \sigma_\gamma(f(c) - c\mu)$, with $f(c) = f_0(c) + \epsilon^2 |\nabla_\Gamma c|^2$, and modifies the surface tension force accordingly for numerical purposes.

The remaining steps are specific to Trace FEM. The sphere Γ is immersed in a cube, which is meshed into tetrahedra [8]. See Fig. 1. The zero level set of the P_1 (i.e., first order polynomial) Lagrangian interpolant (to the vertices of the tetrahedra) of the signed distance function of Γ provides a polyhedral approximation Γ_h of the sphere, which will further be used for numerical integration in the weak formulation instead of Γ . Tetrahedra intersected by Γ_h form an active mesh $\mathcal{T}^{\text{bulk}}$ that supports the degrees of freedom (red layer in Fig. 1). On $\mathcal{T}^{\text{bulk}}$ we further define finite

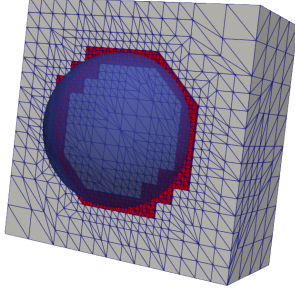


Figure 1: A model liposome (blue) immersed in a bulk tetrahedral mesh (gray) coarser than the actual computational mesh for visualization purposes.

dimensional spaces of continuous functions, which are polynomials of degree either 1 or 2 on each tetrahedra of $\mathcal{T}^{\text{bulk}}$. Let the restrictions of \mathbf{u}_h , p_h , c_h , and μ_h to Γ_h be the approximations of \mathbf{u} , p , c , and μ . Replacing \mathbf{u} , p , c , μ in the integral formulation with \mathbf{u}_h , p_h , c_h , μ_h and choosing the test functions in the corresponding spaces leads to a large (but finite) system of ordinary differential equations (ODEs). Details of the Trace FEM for the NSCH equations on surfaces are given in [45, 29]. The fidelity of the numerical solution is ensured by a sequence of mesh refinements until the solutions on two subsequent meshes demonstrate the same qualitative and quantitative behavior [27, 9]. For the results in this paper we adopted

mesh with 225822 active degrees of freedom (193086 for \mathbf{u}_h and 10912 for p_h , c_h , and μ_h). In order to contain the computational time required by the solution of the system of ODEs, we use time-stepping scheme that (i) decouples the fluid and phase-field equation solvers at each time step [29] and (ii) makes use of an adaptive time stepping technique [13]. The time step Δt adaptively varies from $\Delta t = 4 \times 10^{-6}$ s during the fast initial phase of spinodal decomposition to about $\Delta t = 8 \times 10^{-4}$ s during the later slow phase of lipid domain coarsening and growth, and up to $\Delta t = 4$ s when the process is close to equilibrium. The piecewise polynomial approximations \mathbf{u}_h , p_h , c_h , and μ_h are computed at every time $t^{n+1} = t^n + \Delta t$ till $t^{\text{final}} = 4000$ s.

Just like the method proposed in [46], the finite element method described here produces numerical solutions that satisfy the mass conservation principle behind (1)-(3):

$$\int_{\Gamma_h} c_h(\mathbf{x}, t_n) ds = \int_{\Gamma_h} c_h(\mathbf{x}, t_{n-1}) ds \quad \text{implying} \quad \frac{\int_{\Gamma_h} c_h(\mathbf{x}, t_n) ds}{\int_{\Gamma_h} 1 ds} \simeq a_{\text{ld}} \quad (5)$$

for all $n = 1, \dots, N$. Following [46], we also consider the total perimeter of the lipid domains p_{ld} as a quantity of interest for the quantitative comparison with the experiments. We remark that

numerically p_{ld} is computed as

$$p_{\text{ld}}(t_n) := 2\pi \int_{\Gamma_h} \epsilon |\nabla_{\Gamma} c_h(\mathbf{x}, t_n)|^2 ds. \quad (6)$$

See [46] for more details on this.

3 Results and Discussion

We focused on a ternary membrane composition DOPC:DPPC:Chol, which is known to separate into co-existing liquid ordered (l_o) and liquid disordered (l_d) phases near room temperature when mixed in proper ratios [15, 40]. Upon phase separation, the l_d phase is composed primarily of DOPC and the l_o phase is primarily composed of Chol and DPPC. The relative size of these two phases can be tuned by adjusting the molar ratio of the lipid components. To assess our model of phase separation, we decided to focus our experiments on two membrane compositions that provide distinct and nearly opposite phase-behavior: one composition with majority l_o phase and the other one with a minority l_o phase. We chose membranes composed of DOPC:DPPC:Chol at molar ratio of 1:1:15%, in which the l_o phase is predicted to occupy about 29% of the membrane surface at 25°C and 1:2:25%, in which the l_o phase would occupy about 70% of the membrane area at 15°C. These area fractions were calculated using an approach described in our previous study [46] that relies on the composition of each phase (determined based on the phase diagram tie-lines) and the molecular area of the lipid components. The Cahn–Hilliard model used in [46], as well as continuum based models applied in other studies [43, 25, 36, 23, 12], would predict nearly the same evolution of the domain ripening process for these two compositions since it does not account for in-membrane viscous and transport effects. However, the experimental data presented in this section reveal a different domain ripening dynamics, which can be correctly captured by the more complex NSCH model described in Sec. 2.2.1. Table S1 summarizes the lipid composition of each phase in the examined membranes along with the fraction of lipids in each phase and the membrane area fraction of the ordered phase for the corresponding membranes.

Membrane composition	Liquid ordered (l_o)			Liquid disordered (l_d)			Lipid fraction		Area fraction
DOPC:DPPC:Chol (Temp)	DOPC	DPPC	Chol	DOPC	DPPC	Chol	α_{l_o}	α_{l_d}	a_{ld}
1:1:15% (25°C)	16%	58%	26%	57%	34%	9%	0.35	0.65	29.4%
1:2:25% (15°C)	12%	58%	30%	70%	22%	8%	0.78	0.22	70.4%

Table 2: The composition of lipids in the liquid ordered and disordered phases (based on phase diagram), fraction of lipids in each phase, and the estimated domain area fraction for the two examined membrane compositions.

We applied a modified form of electroformation to produce GUVs of these two compositions and studied phase separation on these GUVs at temperature ranging in [15.8, 17.5]°C for 1:2:25% and

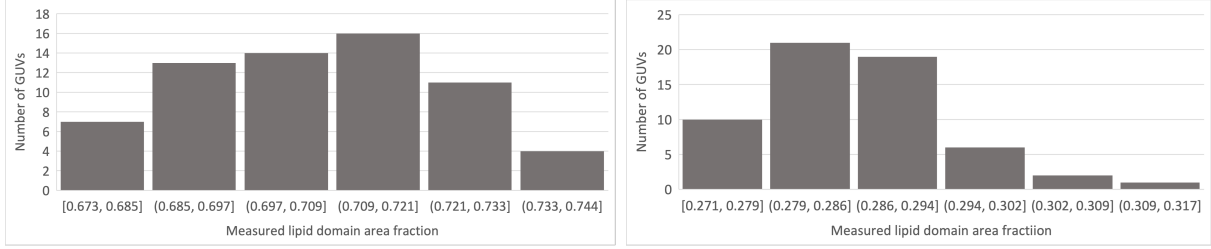


Figure 2: Left: Distribution of experimental measurements of the lipid domain area fraction, with average 0.708 and standard deviation 0.017, for composition 1:2:25%. The total number of measurements is 65 and they are related to 20 GUVs. Right: Distribution of experimental measurements of the lipid domain area fraction with average 0.287 and standard deviation 0.008, for composition 1:1:15%. The total number of measurements is 59 and they are related to 18 GUVs.

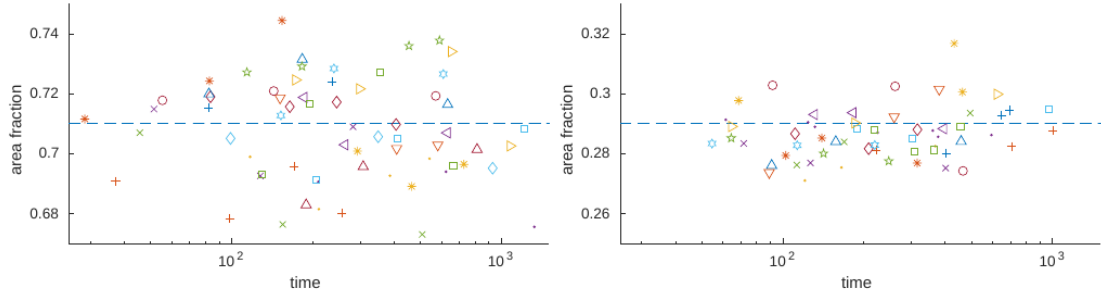


Figure 3: Experimentally measured lipid domain area fraction over time for composition 1:2:25% (left) and 1:1:15% (right). Different markers correspond to different GUVs and the dashed line represents the linear fit to the experimentally measured lipid domain area fractions.

[23.8, 25.7]°C for 1:1:15% composition. Note that the experimental temperature ranges were selected to match the temperatures used for the above-mentioned theoretical calculations. Using confocal fluorescence microscopy, we examined a minimum of 18 GUVs (from 4-5 independent experiments) for the number of their lipid domains as well as area and perimeter of domains at different time points, for each GUV composition. The fraction of vesicle surface area occupied by the l_o phase, i.e. lipid domain area fraction, in GUVs was calculated from the confocal images. The results are summarized in Fig. 2, which shows the distribution of lipid domain area fractions for both GUV compositions. The experimental l_o domain area fractions, 0.287 ± 0.008 and 0.708 ± 0.017 , are in great agreement with those predicted above (Table S1) based on the literature-reported phase diagrams, 0.294 and 0.704, for 1:1:15% and 1:2:25% compositions, respectively. This agreement validates our experimental results. We report in Fig. 3 the experimentally measured lipid domain area fraction over time for the two compositions. We observe only slight (i.e. non-significant)

changes on a given GUV as time passes, i.e. as the number of domains reduces. This result supports one of the assumptions behind the NSCH model, that is the conservation of lipid domain area fraction over time. The time on the horizontal axis in Fig. 3-6 corresponds to the time as measured in the experiments, as is the case for the times reported in Fig. 7 and 8.

Independent of the experimental results, 10 numerical simulations were run for each composition. All the simulated liposomes had a $10\text{ }\mu\text{m}$ diameter and they differed in the realization of the random variable used to set up initial state as explained in Sec. 2.2.1. For each simulation, we tracked the total lipid domain perimeter and the total number of lipid domains in order to compare with the experimental data. The computed lipid domain area fraction is not reported since, as mentioned before, the NSCH model is conservative and thus the lipid domain area fraction stays constant over time.

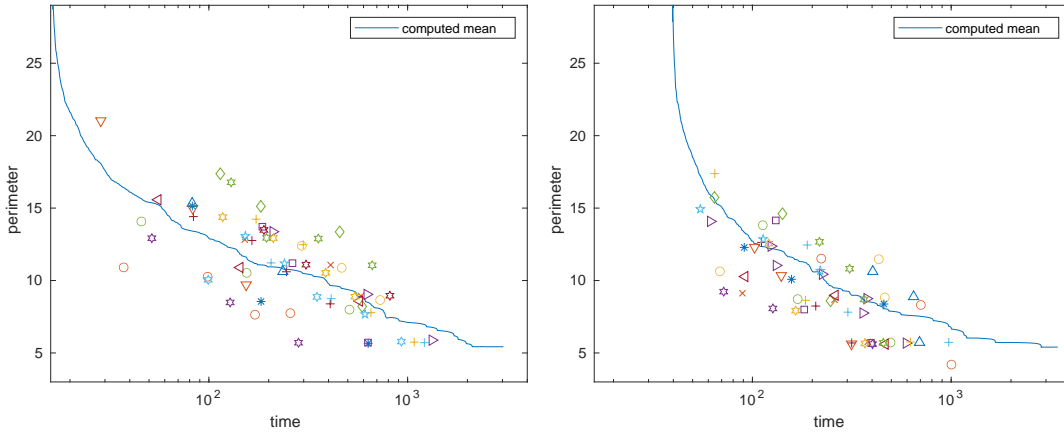


Figure 4: Total lipid domain perimeter in μm over time for composition 1:2:25% (left) and 1:1:15% (right): numerical results average (solid line) and experimental data (markers).

In order to compare the total lipid domain perimeter between simulations and experiments, we first scaled all dimensional observables that depend on a length unit by the radius of the corresponding GUV, since the diameter of GUVs varied in the experiments (between $9\text{--}16\text{ }\mu\text{m}$) while it was constant in the simulations. Fig. 4 reports all the rescaled experimental measurements with markers (a different marker for each GUV) and the average of the computed total lipid domain perimeter from all the simulations with a solid line for compositions 1:2:25% and 1:1:15%. In both cases, the average of the computed total lipid domain perimeters falls within the cloud of experimental measurements. We note that no experimental measurement is available before 40 s because no lipid domains were observed in this time frame, presumably due to the small size of domains that could not be resolved under fluorescence microscopy.

Next, we performed a quantitative comparison for the total number of lipid domains on a GUV over time. Fig. 5 shows the experimentally measured and numerically computed data for both examined compositions. The measurements are reported with a circle, while for the simulations we

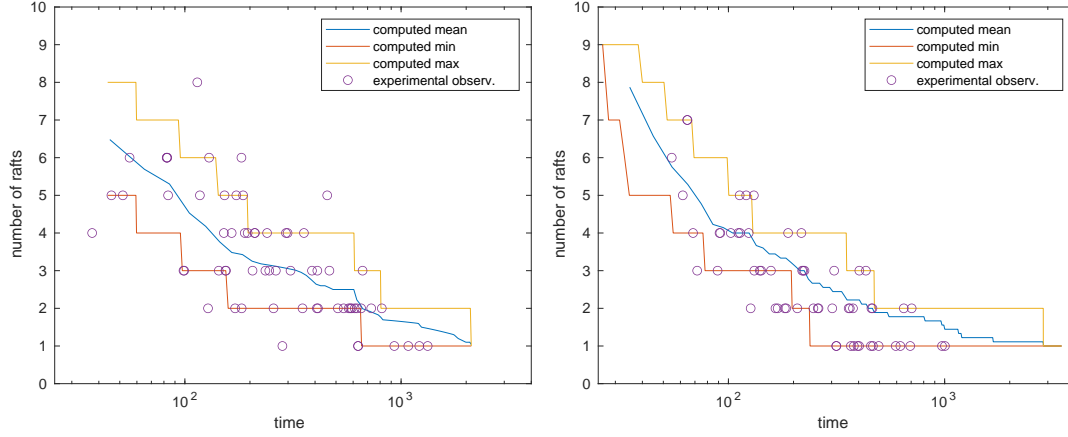


Figure 5: Total number of lipid domains over time for composition 1:2:25% (left) and 1:1:15% (right): numerical results average (solid blue line), minimum and maximum values found numerically (solid orange and yellow lines, respectively), and experimental data (circles).

reported three solid lines corresponding to the numerical results average, minimum, and maximum number of lipid domains found in the simulations. We see that the vast majority of the experimental data (89% for composition 1:2:25% and 91% for composition 1:1:15%) falls within the computed extrema.

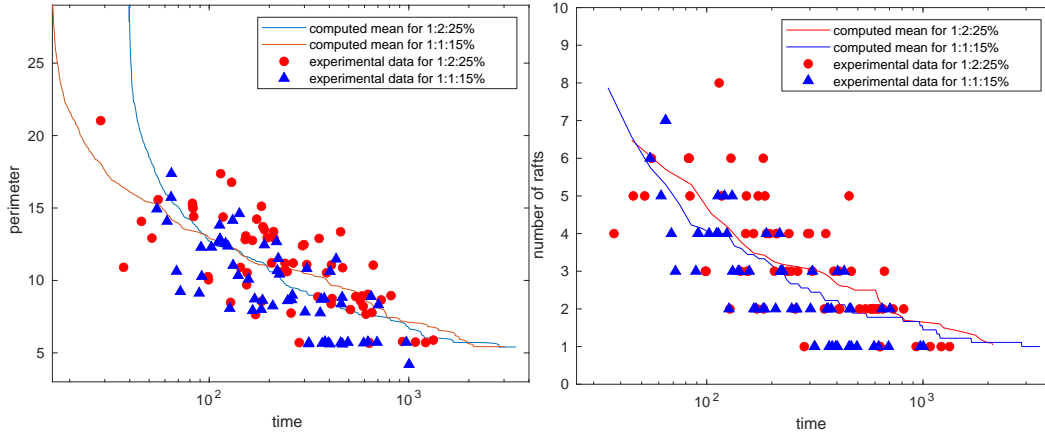


Figure 6: Superimposition of experimental data for composition 1:2:25% (red dots) and 1:1:15% (blue triangles) with the corresponding computed means (solid line with corresponding color) for the total lipid domain perimeter (left) and total number of lipid domains (right).

In order to facilitate the understanding of the different domain ripening dynamics for the two

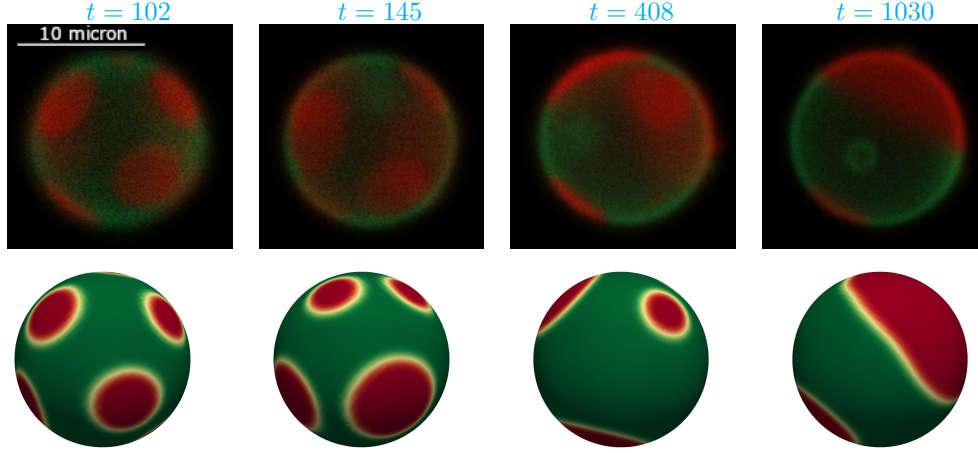


Figure 7: Qualitative comparison for 1:2:25%: epi-fluorescence microscopy images (with black background) and numerical results (with white background) at four different times in time interval $[102, 1030]$ s. Click any picture above to run the full animation of a representative simulation.

membrane compositions under consideration, we superimpose the experimental data for total lipid domain perimeter and total number of lipid domains in Fig. 6. We observe in average faster dynamics towards the equilibrium state (i.e., one domain of the minority phase within a background of the majority phase) for composition 1:1:15%, which has majority l_d phase. This is correctly captured by the NSCH model described in Sec. 2.2.1. Indeed, we see that the solid blue curve (corresponding to the computed mean for composition 1:1:15%) lies below the red curve (corresponding to the computed mean for composition 1:2:25%) for the majority of the time interval under consideration in both graphs in Fig. 6. We recall that the simplified model in [46] would predict the same evolution for $a_{ld} = 0.71$ and $a_{ld} = 0.29$ and thus it would be unsuited to reproduce the experimental data reported in this paper.

To further compare the experimental data to the simulation results, we present a qualitative comparison between images acquired with epi-fluorescence microscopy and images obtained from post-processing the numerical results. Fig. 7 and Fig. 8 present such comparison for compositions 1:2:25% and 1:1:15%, respectively. Notice that the representative microscopy images in Fig. 7 and 8 refer to different sets of GUVs than those used for the quantitative analysis in Fig. 2-5 because confocal microscopy (needed for the measurement) and epi-fluorescence microscopy cannot be used simultaneously. Overall, from Fig. 7 and 8 we see an excellent qualitative agreement between experiments and simulations.

A piece of information that is provided by the numerical simulations but is impossible to visualize or measure experimentally is the flow field. Fig. 9 shows the evolution of the computed velocity vectors superimposed to the computed surface fraction for both compositions. We observe a larger

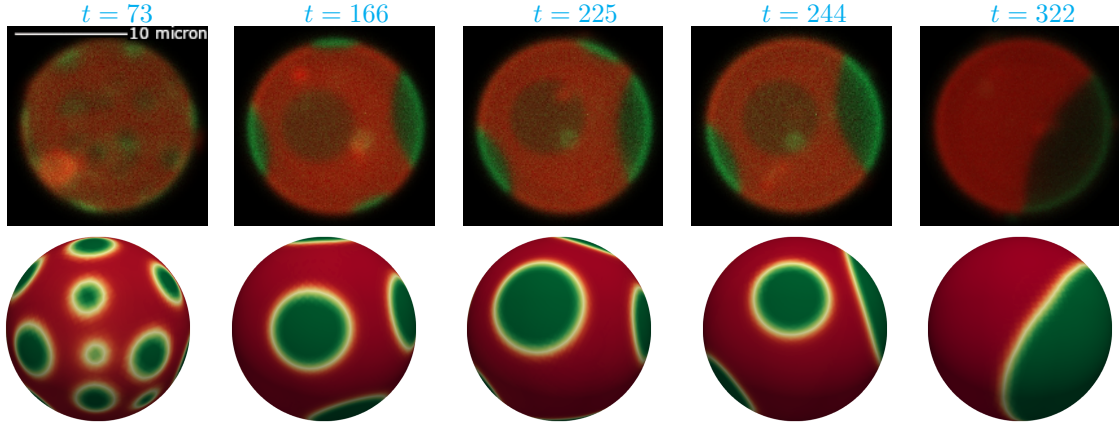


Figure 8: Qualitative comparison for 1:1:15%: epi-fluorescence microscopy images (with black background) and numerical results (with white background) at five different times in time interval [73, 322] s. Click any picture above to run the full animation of a representative simulation.

velocity magnitude when there are several lipid domains on the surface that are in the process of merging. The velocity magnitude becomes smaller as the number of lipid domain decreases and the system gets closer to an equilibrium.

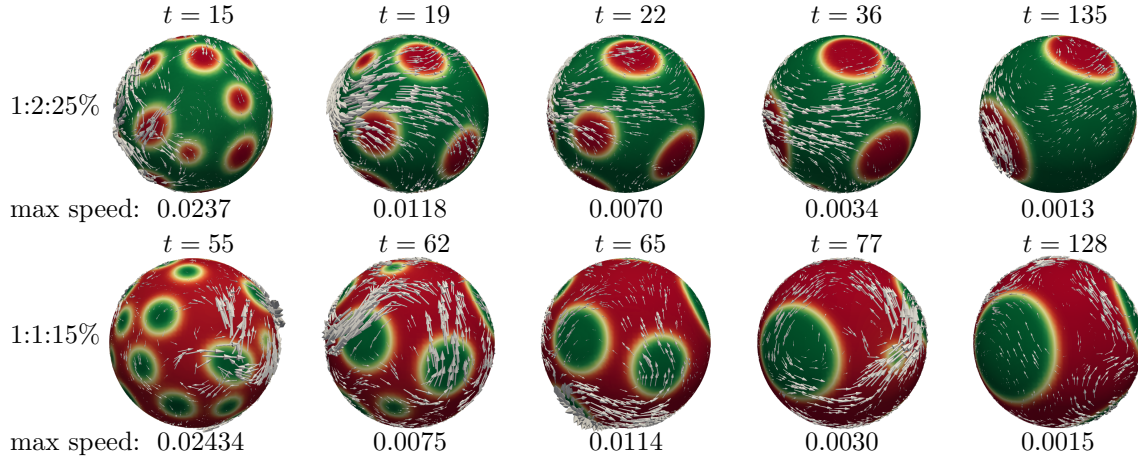


Figure 9: Composition 1:2:25%: Evolution of the velocity vectors superimposed to the lipid domains and maximum speed in $\mu\text{m/s}$ for composition 1:2:25% (top) and 1:1:15% (bottom). The velocity vectors are magnified by a factor 100, 300, 300, 700, and 1500 (from left to right) for visualization purposes.

Interestingly, in the case of composition 1:2:25%, we observed different types of domain forma-

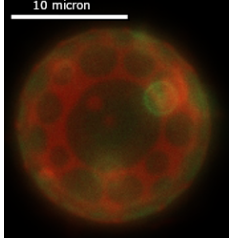


Figure 10: Composition 1:2:25%: formation of l_o domains (green) within the l_d phase (red).

tion on GUVs. While at equilibrium these GUVs consistently had a l_o phase that occupied the majority of their surface (in average 70.8%), prior to the equilibrium state, three distinct domain patterns were observed on these GUVs. In some GUVs, l_d domains formed within the l_o phase (i.e., red patches on green background as shown in Fig. 7), in others l_o domains formed within the l_d phase (i.e. green patches on red background, see Fig. 10), and in others again a combination of these domain patterns was detected (see Fig. 11). Often, the dominating phase in the membrane forms the background in which domains of the minority phase form, merge, and grow into one larger domain at equilibrium. Domain formation in our GUVs with 1:1:15% composition always followed this typical phase behavior. However, in some compositions such as 1:2:25%, it is also possible that the dominating phase forms domains within the minority phase [32]. Thus, membranes of such compositions may show either type of domains. The rather rare formation of domains of the dominating

phase within the minority phase background may be due to the existence of a metastable third phase for such membrane compositions, which could be due to the formation of some temporary molecular complexes. It can be seen as an example of the Ostwald rule of stages, by which the system may go through a sequence of intermediate states before reaching the most energetically preferable one [39, 2]. The metastable phase does not present as an equilibrium state (i.e., the states reported in phase diagrams), nonetheless it can exist long enough to influence the dynamics of the phases. For instance, the presence of such third phase can cause variations in domain area fraction before reaching a two-phase equilibrium state. In fact, we noticed that in those GUVs that formed l_o domains within l_d phase in 1:2:25% composition, the area fraction of l_o phase was not as stable and varied prior to equilibrium; the l_o domain area fraction was on average $\sim 6\%$ lower than that at equilibrium.

The CHNS model (1)-(3) is not suitable to model the dynamic of a third temporary phase. Even reproducing the reverse phase pattern in the numerical simulations proved to be challenging as the initial conditions formulated in Sec. 2.2.1 would inevitably lead to l_d domains formed within the l_o phase for composition 1:2:25%. In an effort to emulate the effect of the metastable phase on the pattern evolution, we introduced the following 2 changes with respect to the set up described in Sec. 2.2.1: i) the simulations are started with a number of preformed l_o domains placed symmetrically in l_d background and ii) the area fraction of l_o phase is reduced by about 6% to match experimental evidence. Fig. 12 shows the formation of l_o domains within the l_d phase starting from 12 symmetrically placed l_o domains and $a_{ld} = 0.64$. The third scenario (coexistence of l_o and l_d domains) is shown in Fig. 13 and was obtained starting from 6 symmetrically placed l_o domains and $a_{ld} = 0.65$. Because of the forced initial condition described at the above point i), which differ from the initial composition in the experiments (i.e., a initially homogenous GUV), we preferred

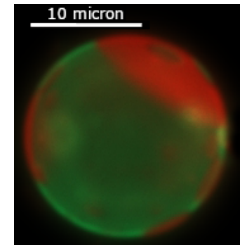


Figure 11: Composition 1:2:25%: combination of l_d domains (red) within the l_o phase (green) and viceversa.

not to report time in Fig. 12 and 13.

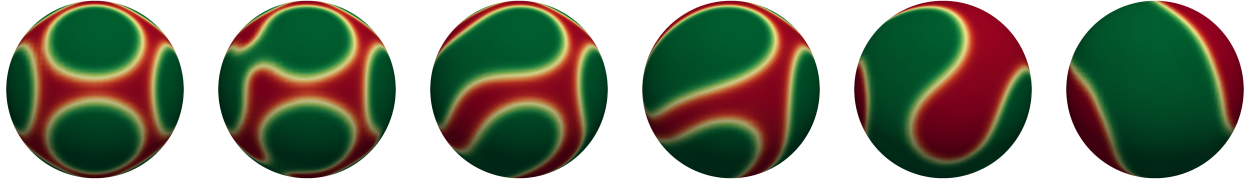


Figure 12: Composition 1:2:25%: simulated evolution of l_o domains (green) within the l_d phase (red) starting from 12 symmetrically placed l_o domains and $a_{ld} = 0.64$. Time is increasing from left to right.

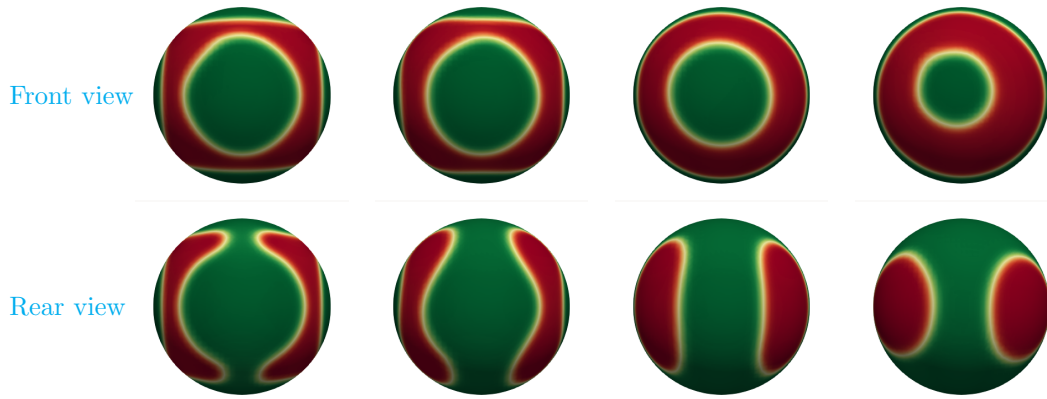


Figure 13: Composition 1:2:25%: front (top row) and rear (bottom row) view of a simulated GUV showing mixed l_o (green) and l_d (red) domains starting from 6 symmetrically placed l_o domains and $a_{ld} = 0.65$. Time is increasing from left to right. Click any picture above to run the full animation.

4 Conclusion

This paper presents an experimental and computational study on the evolution of lipid rafts in membranes with ternary membrane composition DOPC:DPPC: Chol. We focused on two specific compositions that yield opposite and nearly inverse phase behavior. A non-equilibrium thermodynamics model describing phase separation alone, like the Cahn–Hilliard model, would predict nearly the same evolution of the domain ripening process for these two compositions. However, our exper-

imental data collected using fluorescence microscopy reveal different domain ripening dynamics. In order to capture this phenomenon, we considered the more complex Navier–Stokes–Cahn–Hilliard model, which accounts for in-membrane viscous and transport effects. The computational results obtained with this improved model are in excellent agreement with the experimental data in terms of domain area fraction, total domain perimeter over time and total number of domains over time for both compositions under consideration.

Acknowledgments

This work was partially supported by US National Science Foundation (NSF) through grant DMS-1953535. M.O. acknowledges the support from NSF through DMS-2011444. S.M. acknowledges the support from NSF through DMR-1753328. A.Q. acknowledges support from the Radcliffe Institute for Advanced Study at Harvard University where she has been a 2021-2022 William and Flora Hewlett Foundation Fellow. The authors are grateful to Vassiliy Lubchenko for insightful discussions on thermodynamics of polymorphs and to Alexander Zhiliakov for helping with the set up of the numerical experiments.

References

- [1] H. Abels, H. Garcke, and G. Grün. Thermodynamically consistent, frame indifferent diffuse interface models for incompressible two-phase flows with different densities. *Mathematical Models and Methods in Applied Sciences*, 22(03):1150013, 2012.
- [2] Valerie J Anderson and Henk NW Lekkerkerker. Insights into phase transition kinetics from colloid science. *Nature*, 416(6883):811–815, 2002.
- [3] A. Bandekar and S. Sofou. Floret-shaped solid domains on giant fluid lipid vesicles induced by pH. *Langmuir*, 28:4113–4122, 2012.
- [4] Amey Bandekar, Charles Zhu, Ana Gomez, Monica Zofia Menzenski, Michelle Sempkowski, and Stavroula Sofou. Masking and triggered unmasking of targeting ligands on liposomal chemotherapy selectively suppress tumor growth in vivo. *Molecular Pharmaceutics*, 10(1):152–160, 2013.
- [5] W.F. Drew Bennett and D. Peter Tieleman. Computer simulations of lipid membrane domains. *Biochimica et Biophysica Acta (BBA) - Biomembranes*, 1828(8):1765–1776, 2013.
- [6] D.A. Brown and E. London. Structure and function of sphingolipid- and cholesterol-rich membrane rafts. *J Biol Chem.*, 275(23):17221–17224, 2000.

- [7] R.E. Brown. Sphingolipid organization in biomembranes: what physical studies of model membranes reveal. *Journal of Cell Science*, 111(1):1–9, 1998.
- [8] Philippe G Ciarlet. *The finite element method for elliptic problems*, volume 40. SIAM, 2002.
- [9] Charles M Elliott and Stig Larsson. Error estimates with smooth and nonsmooth data for a finite element method for the Cahn–Hilliard equation. *Mathematics of Computation*, 58(198):603–630, 1992.
- [10] Lawrence C Evans. *Partial differential equations*, volume 19. American Mathematical Soc., 2010.
- [11] M. Fidorra, A. Garcia, J.H. Ipsen, S. Härtel, and L.A. Bagatolli. Lipid domains in giant unilamellar vesicles and their correspondence with equilibrium thermodynamic phases: A quantitative fluorescence microscopy imaging approach. *Biochimica et Biophysica Acta (BBA) - Biomembranes*, 1788(10):2142 – 2149, 2009. Includes Special Section: Cardiolipin.
- [12] Chloe M. Funkhouser, Francisco J. Solis, and K. Thornton. Dynamics of coarsening in multicomponent lipid vesicles with non-uniform mechanical properties. *The Journal of Chemical Physics*, 140(14):144908, 2014.
- [13] Héctor Gómez, Victor M Calo, Yuri Bazilevs, and Thomas JR Hughes. Isogeometric analysis of the Cahn–Hilliard phase-field model. *Computer Methods in Applied Mechanics and Engineering*, 197(49-50):4333–4352, 2008.
- [14] P. Heftberger, B. Kollmitzer, A.A. Rieder, H. Amenitsch, and G. Pabst. In situ determination of structure and fluctuations of coexisting fluid membrane domains. *Biophys J.*, 108(4):854–862, 2015.
- [15] Janos Juhasz, James H Davis, and Frances J Sharom. Fluorescent probe partitioning in giant unilamellar vesicles of 'lipid raft' mixtures. *The Biochemical journal*, 430(3):415–423, September 2010.
- [16] N. Kahya, D. Scherfeld, K. Bacia, B. Poolman, and P. Schuille. Probing lipid mobility of raft-exhibiting model membranes by fluorescence correlation spectroscopy. *J Biol Chem.*, 278(30):28109–15, 2003.
- [17] You Jung Kang, Harrison S Wostein, and Sheereen Majd. A simple and versatile method for the formation of arrays of giant vesicles with controlled size and composition. *Advanced Materials*, 25(47):6834–6838, 2013.
- [18] Andrey S. Klymchenko and Remy Kreder. Fluorescent probes for lipid rafts: From model membranes to living cells. *Chemistry & Biology*, 21(1):97 – 113, 2014.

- [19] Benjamin Kollmitzer, Peter Heftberger, Michael Rappolt, and Georg Pabst. Monolayer spontaneous curvature of raft-forming membrane lipids. *Soft Matter*, 9:10877–10884, 2013.
- [20] Peter I. Kuzmin, Sergey A. Akimov, Yuri A. Chizmadzhev, Joshua Zimmerberg, and Fredric S. Cohen. Line tension and interaction energies of membrane rafts calculated from lipid splay and tilt. *Biophysical Journal*, 88(2):1120–1133, 2005.
- [21] L.D. Landau and E.M. Lifshitz. *Statistical physics*. Oxford: Pergamon, 1958.
- [22] I. Levental, K.R. Levental, and F.A. Heberle. Lipid rafts: Controversies resolved, mysteries remain. *Trends Cell Biol.*, 30(5):341–353, 2020.
- [23] Shuwang Li, John Lowengrub, and Axel Voigt. Locomotion, wrinkling, and budding of a multicomponent vesicle in viscous fluids. *Communications in Mathematical Sciences*, 10:645–670, 2012.
- [24] Daniel Lingwood and Kai Simons. Lipid rafts as a membrane-organizing principle. *Science*, 327(5961):46–50, 2010.
- [25] John S Lowengrub, Andreas Rätz, and Axel Voigt. Phase-field modeling of the dynamics of multicomponent vesicles: Spinodal decomposition, coarsening, budding, and fission. *Physical Review E*, 79(3):031926, 2009.
- [26] Sheereen Majd and Michael Mayer. Hydrogel stamping of arrays of supported lipid bilayers with various lipid compositions for the screening of drug–membrane and protein–membrane interactions. *Angewandte Chemie*, 117(41):6855–6858, 2005.
- [27] Maxim A Olshanskii, A. Reusken, and J. Grande. A finite element method for elliptic equations on surfaces. *SIAM Journal on Numerical Analysis*, 47:3339–3358, 2009.
- [28] Maxim A Olshanskii and Arnold Reusken. Trace finite element methods for PDEs on surfaces. In *Geometrically Unfitted Finite Element Methods and Applications*, pages 211–258. Springer, 2017.
- [29] Yerbol Palzhanov, Alexander Zhiliakov, Annalisa Quaini, and Maxim Olshanskii. A decoupled, stable, and linear fem for a phase-field model of variable density two-phase incompressible surface flow. *Computer Methods in Applied Mechanics and Engineering*, 387:114167, 2021.
- [30] SooHyun Park and Sheereen Majd. Reconstitution and functional studies of hamster p-glycoprotein in giant liposomes. *PloS one*, 13(6):e0199279, 2018.
- [31] H Jelger Risselada and Siewert J Marrink. The molecular face of lipid rafts in model membranes. *Proceedings of the National Academy of Sciences*, 105(45):17367–17372, 2008.

- [32] Yuka Sakuma, Toshihiro Kawakatsu, Takashi Taniguchi, and Masayuki Imai. Viscosity landscape of phase-separated lipid membrane estimated from fluid velocity field. *Biophysical Journal*, 118(7):1576–1587, 2020.
- [33] Michelle Sempkowski, Charles Zhu, Monica Zofia Menzenski, Ioannis G. Kevrekidis, Frank Bruchertseifer, Alfred Morgenstern, and Stavroula Sofou. Sticky patches on lipid nanoparticles enable the selective targeting and killing of untargetable cancer cells. *Langmuir*, 32(33):8329–8338, 2016.
- [34] Stefan Semrau and Thomas Schmidt. Membrane heterogeneity – from lipid domains to curvature effects. *Soft Matter*, 5:3174–3186, 2009.
- [35] Erdinc Sezgin, Ilya Levental, Michal Grzybek, Günter Schwarzmann, Veronika Mueller, Alf Honigsmann, Vladimir N. Belov, Christian Eggeling, Ünal Coskun, Kai Simons, and Petra Schwille. Partitioning, diffusion, and ligand binding of raft lipid analogs in model and cellular plasma membranes. *Biochimica et Biophysica Acta (BBA) - Biomembranes*, 1818(7):1777 – 1784, 2012.
- [36] Jin Sun Sohn, Yu-Hau Tseng, Shuwang Li, Axel Voigt, and John S Lowengrub. Dynamics of multicomponent vesicles in a viscous fluid. *Journal of Computational Physics*, 229(1):119–144, 2010.
- [37] Cynthia A Stanich, Aurelia R Honerkamp-Smith, Gregory Garbes Putzel, Christopher S Warth, Andrea K Lamprecht, Pritam Mandal, Elizabeth Mann, Thien-An D Hua, and Sarah L Keller. Coarsening dynamics of domains in lipid membranes. *Biophysical journal*, 105(2):444–454, 2013.
- [38] Andrea N. Tremontozzi, Zachary I. Imam, Morgan Mendicino, Carl C. Hayden, and Jeanne C. Stachowiak. Liposome-mediated chemotherapeutic delivery is synergistically enhanced by ternary lipid compositions and cationic lipids. *Langmuir*, 35(38):12532–12542, 2019.
- [39] RA Van Santen. The ostwald step rule. *The Journal of Physical Chemistry*, 88(24):5768–5769, 1984.
- [40] Sarah L Veatch and Sarah L Keller. Separation of liquid phases in giant vesicles of ternary mixtures of phospholipids and cholesterol. *Biophysical journal*, 85(5):3074–3083, 2003.
- [41] Sarah L. Veatch, Olivier Soubias, Sarah L. Keller, and Klaus Gawrisch. Critical fluctuations in domain-forming lipid mixtures. *Proceedings of the National Academy of Sciences*, 104(45):17650–17655, 2007.
- [42] Š. Bálint and M.L. Dustin. Localizing order to boost signaling. *eLife*, 6:e25375, 2017.

- [43] Xiaoqiang Wang and Qiang Du. Modelling and simulations of multi-component lipid membranes and open membranes via diffuse interface approaches. *Journal of Mathematical Biology*, 56(3):347–371, Mar 2008.
- [44] O. Wesolowska, K. Michalak, J Maniewska, and A. B. Hendrich. Giant unilamellar vesicles - a perfect tool to visualize phase separation and lipid rafts in model systems. *Acta Biochimica Polonica*, 56:33–39, 2009.
- [45] Vladimir Yushutin, Annalisa Quaini, Sheereen Majd, and Maxim Olshanskii. A computational study of lateral phase separation in biological membranes. *International journal for numerical methods in biomedical engineering*, 35(3):e3181, 2019.
- [46] Alexander Zhiliakov, Yifei Wang, Annalisa Quaini, Maxim Olshanskii, and Sheereen Majd. Experimental validation of a phase-field model to predict coarsening dynamics of lipid domains in multicomponent membranes. *Biochimica et Biophysica Acta (BBA)-Biomembranes*, 1863(1):183446, 2021.
- [47] Jingzhi Zhu, Long-Qing Chen, Jie Shen, and Veena Tikare. Coarsening kinetics from a variable-mobility Cahn-Hilliard equation: Application of a semi-implicit Fourier spectral method. *Phys. Rev. E*, 60:3564–3572, Oct 1999.

Supplementary material to the article titled: “Lipid domain coarsening and fluidity in multicomponent lipid vesicles: A continuum based model and its experimental validation”

To estimate the surface density of each phase, we first calculated the molar-weighted average values for the molecular weight (MW) and the molecular surface area (A) for the corresponding phase, and calculated the surface density by:

$$\rho = \frac{MV}{A}.$$

The average MW for each phase was calculated using its lipid composition, as summarized in Table 2, and the molecular weight of individual lipids (785.593 g/mol for DOPC, 733.562 g/mol for DPPC and 386.65 g/mol for chol). Similarly, the average value of A for each phase was found based on its lipid composition and cross-sectional area of its lipid components. The cross-sectional area of lipids were estimated using an approach detailed in our previous study [46]. Table S1 summarizes the calculated values.

Membrane composition	Average MW		Average A		$\rho = MV/A$	
DOPC:DPPC:Chol (Temp)	l_d	l_o	l_d	l_o	l_d	l_o
1:2:25% (15°C)	742.231	635.732	63.156	43.346	$1.951e - 23$	$2.435e - 23$
1:2:25% (17.5°C)	741.190	640.242	63.271	44.618	$1.945e - 23$	$2.382e - 23$
1:1:15% (22.5°C)	742.057	649.609	63.300	46.366	$1.946e - 23$	$2.326e - 23$
1:1:15% (25°C)	739.587	651.689	62.479	47.603	$1.965e - 23$	$2.273e - 23$

Table S1: The average molecular weight (MW) and molecular surface area (A) of lipids in each phase, and the surface density of the corresponding phase (ρ) in the examined membrane compositions at different temperatures. Molecular weight (MW) is presented in Kg/mol, A in \AA , and ρ in $\text{g}/\text{\AA}^2$.